Geophysical Research Letters

RESEARCH LETTER
10.1029/2025GL119915

Upper Mantle Heterogeneity and Weak Subduction Boundaries Control Crustal Stress in the Korean Peninsula

Sungho Lee[1], Chang Soo Cho[2], YoungHee Kim[3], Youngsang Kwon[4], and Eunseo Choi[5]

[1]Earthquake Research Center, Korea Institute of Geoscience and Mineral Resources, Daejeon, Republic of Korea, [2]Integrated Earthquake Monitoring Research Center, Korea Institute of Geoscience and Mineral Resources, Daejeon, Republic of Korea, [3]School of Earth and Environmental Sciences, Seoul National University, Seoul, Republic of Korea, [4]Department of Earth Sciences, The University of Memphis, Memphis, TN, USA, [5]Center for Earthquake Research and Information, The University of Memphis, Memphis, TN, USA

Key Points:

- Upper-mantle buoyancy and weak subduction zones explain Korea's intraplate earthquakes, while lithospheric variations alone fall short
- The subducted Pacific slab in the mantle transition zone is essential for generating the observed east–west compressive stress
- The east–west stress pattern emerges without far-field compression, driven by upper-mantle heterogeneity and weak plate boundaries

Supporting Information:

Supporting Information may be found in the online version of this article.

Correspondence to:

S. Lee,
slee91@kigam.re.kr

Citation:

Lee, S., Cho, C. S., Kim, Y., Kwon, Y., & Choi, E. (2026). Upper mantle heterogeneity and weak subduction boundaries control crustal stress in the Korean Peninsula. *Geophysical Research Letters*, *53*, e2025GL119915. https://doi.org/10.1029/2025GL119915

Received 9 OCT 2025
Accepted 24 FEB 2026

Author Contributions:

Conceptualization: Sungho Lee
Investigation: Sungho Lee, Chang Soo Cho, Youngsang Kwon
Methodology: Sungho Lee
Supervision: Sungho Lee
Visualization: Sungho Lee, Chang Soo Cho
Writing – original draft: Sungho Lee, Chang Soo Cho, YoungHee Kim
Writing – review & editing: Sungho Lee, Chang Soo Cho, YoungHee Kim, Youngsang Kwon, Eunseo Choi

Abstract Most earthquakes occur at plate boundaries, but some also strike within stable continental interiors. Although dominant causes of such intraplate earthquakes remain elusive, a prevailing hypothesis attributes intraplate stress and seismicity to variations in lithospheric thickness. Here, we test this hypothesis using the Korean Peninsula as a natural laboratory by constructing three-dimensional numerical models that extend from the surface to a depth of 650 km, incorporating realistic plate boundary configurations and deep thermal and compositional heterogeneities. Our results show that lithospheric thickness variations alone cannot account for the observed seismicity distribution and stress orientations. Instead, models that include weak subduction interfaces, slabs extending into the transition zone, and mantle buoyancy—while excluding shallow lithospheric density contrasts—explain the observed seismicity and stress distribution. In particular, the subducted Pacific slab in the mantle transition zone acts as a gravitational sinker, enhancing crustal compression along the eastern margin of the peninsula.

Plain Language Summary Damaging earthquakes can occur even in stable continental interiors, far from plate boundaries, but their causes are not well understood. One idea is that variations in the thickness of the Earth's rigid outer layer (the lithosphere) create stresses that lead to these intraplate earthquakes. We tested this idea using the Korean Peninsula as an example. We built 3D models from the surface down to 650 km, including tectonic plate boundaries and variations in deep Earth density and viscosity. Our results show that lithospheric thickness variations alone cannot explain the locations of earthquakes or the observed tectonic stress orientation in Korea. However, when we included two key factors, the models did match observations: (a) weak zones along subduction boundaries (where the Pacific and Philippine Sea plates sink into the mantle) and (b) a heavy, cold slab of the Pacific plate lying deep in the mantle (410–660 km) that pulls surrounding material downward. These deep forces, combined with the weak plate boundary zones, compress the crust of Korea from east to west, producing the observed pattern of earthquakes. This suggests that even in stable regions, deep mantle structures and plate boundary effects play a major role in controlling earthquakes.

1. Introduction

Deformation within stable continental interiors is controlled not only by plate interactions (collision, divergence, and subduction) but also by several factors, including variations in lithospheric thickness and strength (Bott et al., 2024; Cao & Liu, 2024; S. Lee et al., 2022, 2025; Mooney et al., 2012), density structure (Becker et al., 2015; Ghosh & Holt, 2012; Ghosh et al., 2013; Hightower et al., 2024; Levandowski et al., 2017; Lithgow-Bertelloni & Guynn, 2004; Saxena et al., 2021), inherited tectonic fabrics (Baird et al., 2010; Powell et al., 1994; Tarayoun et al., 2019), thermal anomalies (Holford et al., 2011), pore-fluid processes (Mishra & Zhao, 2003; Tary et al., 2021), and surface loading changes driven by erosion (Calais et al., 2010), snowfall (Heki, 2003), or glacial cycles (Arvidsson, 1996).

Intraplate earthquakes rarely have a single cause; they result from multiple interacting mechanisms. For example, Bott et al. (2024) showed that variations in lithospheric strength, thickness, and density are essential to seismicity in Western and Central Europe, because pre-existing structures, boundary forces, or post-glacial adjustments cannot fully explain it. Similarly, US studies (e.g., Becker et al., 2015; Hightower et al., 2024) highlight the critical role of upper-mantle heterogeneities in controlling intraplate seismicity.

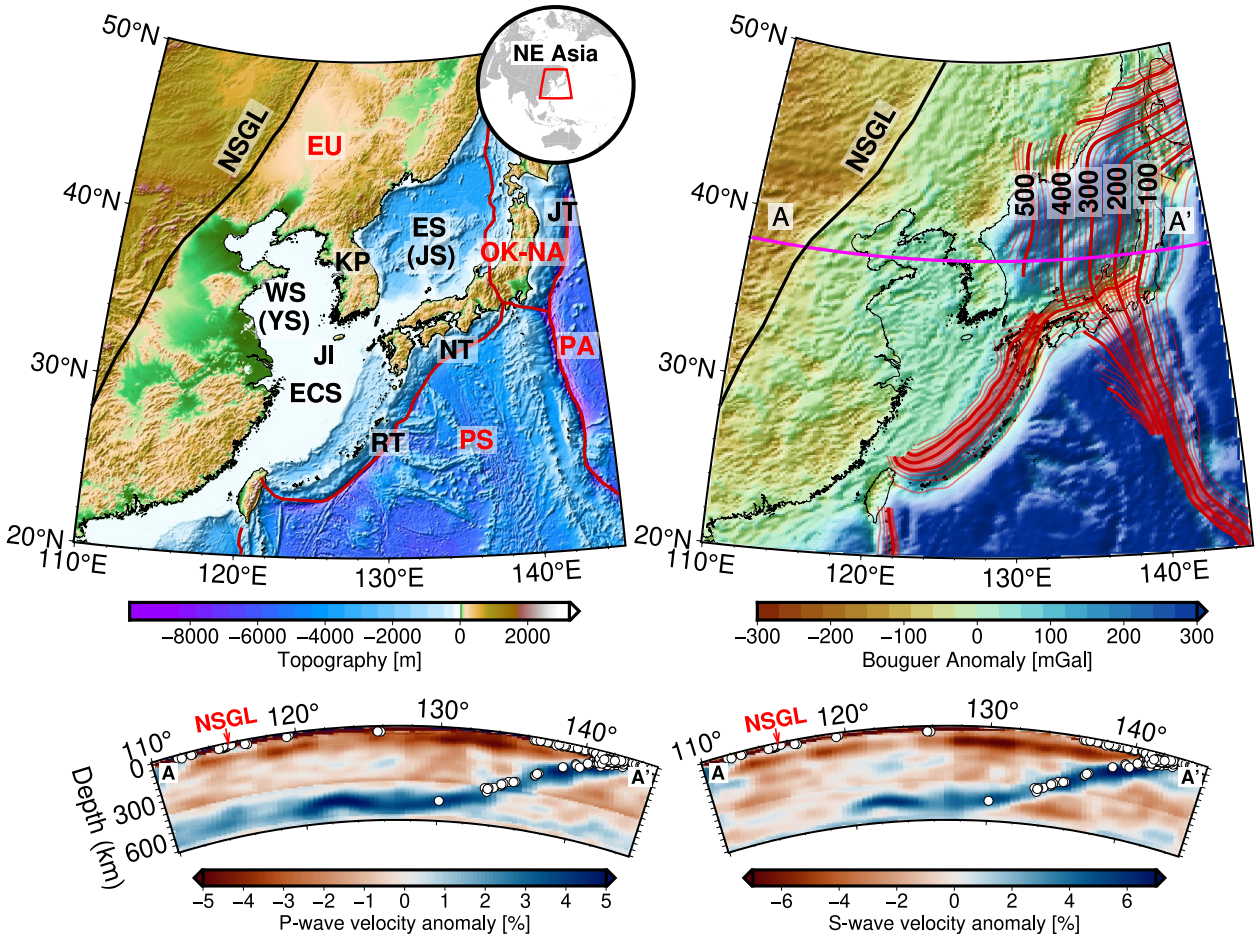

Figure 1. (a) Map of Northeast Asia and its topography. Solid red lines denote plate boundaries, while red saw-toothed lines indicate convergent plate boundaries (Bird, 2003). The black line represents the North-South Gravity Lineament. Geographic references–EU: Eurasian Plate, OK-NA: Okhotsk-North American Plate, PA: Pacific Plate, PS: Philippine Sea Plate, RT: Ryukyu Trench, NT: Nankai Trough, JT: Japan Trench, KP: Korean Peninsula, WS: West Sea (YS: Yellow Sea), ES: East Sea (JS: Sea of Japan), ECS: East China Sea, and JI: Jeju Island. (b) Bouguer gravity anomalies from the EGM08 model (Pavlis et al., 2012) in Northeast Asia. The depths of subducting PA and PS slabs are shown with red contours at 20-km (thin red) and 100-km (thick red) intervals, based on the Slab2.0 model (Hayes et al., 2018). (c, d) Vertical cross-sections of isotropic *P*- and *S*-wave tomography (Tao et al., 2018) along 38°N (cross-section line AA' shown in panel (b)), with earthquakes (white dots) ±1°N from the ISC-GEM catalog, version 11 (Di Giacomo et al., 2018).

Because the lithosphere provides much of the upper mantle's strength, it is a key control on earthquake potential (Mooney et al., 2012). Seismic tomography reveals that regions with fast shear-wave anomalies at 100–200 km depth—typically interpreted as cold, strong lithospheric mantle—rarely host $M \geq 6$ earthquakes, also scarce in cratonic interiors (Mooney et al., 2012; Wesnousky & Scholz, 1980).

S. Lee et al. (2022) found that a geodynamic model with upper mantle heterogeneity reproduced seismicity distribution on the Korean Peninsula (KP) but failed to match observed east–west stress orientations (Rhie & Kim, 2010; Soh et al., 2018). Adding far-field compression resolved this mismatch but produced new inconsistencies, implying the limits of lithospheric-only models and the need for additional factors such as deeper mantle or plate-boundary influences.

The interplay of lithospheric structure and far-field tectonic forces in Northeast Asia highlights the need to re-examine the limitations of existing geodynamic models. The KP, bordered by the Pacific (PA) and Philippine Sea (PS) plates (Figure 1a), is a slowly deforming intraplate region with strain rates of 10^{-15}–10^{-16} s^{-1} (Hao et al., 2019; Jin et al., 2006; Kreemer et al., 2014; S. Lee et al., 2025; Wang & Shen, 2020). GNSS data show deformation mainly driven by the India–Eurasia collision and PA subduction, with minor PS contribution (Hao et al., 2019).

As strain localization and velocity deviations often result from rheological weakness driven by high temperatures, strain rates, low effective friction, or weakening history of past deformation (Fuchs & Becker, 2022; Lambert et al., 2021; Saxena et al., 2023), the KP—being closer to the Ryukyu Trench (~600 km) than to the Japan Trench (~1,000 km) (Figure 1a)—may be more strongly influenced by the PS subduction. Nevertheless, the role of adjacent weak plate boundaries in controlling the stress regime and deformation pattern of the KP remains poorly understood.

Seismic tomography shows the subducted PA slab extends ~1,000 km and lies flat in the transition zone (Fukao et al., 1992; van der Hilst et al., 1991). Improved data sets have refined this stagnant slab image (Huang & Zhao, 2006; Y. Kim et al., 2021; S.-H. Lee et al., 2014; Obayashi et al., 2006, 2009, 2013; Schaeffer & Lebedev, 2013; Tang et al., 2014; Tao et al., 2018; Xi et al., 2024; Zhao, 2004). Its correlation with deep-focus earthquakes confirms it as a coherent feature (Figures 1c and 1d).

Across the circum-Pacific, slabs show four stages: stagnation at 660 km, penetration, trapping at 660–1,000 km, or deeper descent (Fukao & Obayashi, 2013). The PA slab under Northeast Asia exemplifies stagnation (Stage I). The North-South Gravity Lineament—long-wavelength positive Bouguer anomalies—aligns with the slab (Figures 1b–1d), implying that its gravitational pull affects mantle flow and crustal stress.

These observations raise a key question: to what extent do upper mantle structures contribute to stress state in the overlying crust? Specifically, is the intraplate crustal stress field more strongly influenced by shallow structures, such as variations in lithospheric thickness, or by deeper structures like the stagnant slab in the mantle transition zone?

To address the questions raised above, we construct 3D instantaneous mantle convection models incorporating plate boundaries and thermal heterogeneity. By testing different plate boundary configurations and depth-dependent thermal anomalies, we investigate shallow versus deep contributions, including gravitational effects of the stagnant PA slab.

Comparing modeled outputs with stress orientations derived from stress inversion of moment tensors and seismicity density allows us to quantify the roles of PA/PS boundaries, mantle structures, and temperature-dependent variations in lithospheric density, viscosity, and thickness. Our findings emphasize the critical roles of plate boundary weak zones and integrated buoyancy forces in the upper mantle below the lithosphere—including the contribution of the subducting Pacific slab in the mantle transition zone—in shaping regional stress patterns, improving our understanding of intraplate seismicity in the KP and beyond.

2. Materials and Methods

We performed 3D instantaneous mantle convection simulations using the open-source finite element code ASPECT v2.5.0 (Bangerth et al., 2023; Heister et al., 2017; Kronbichler et al., 2012) under the Boussinesq approximation. The models covered the KP region (110°E–145°E, 20°N–50°N, down to 650 km depth), discretized at ~0.125° laterally and 25 km vertically. The shallow 50 km was treated as an effective lithospheric layer with thickness-averaged density from CRUST1.0 (Laske et al., 2013), while prescribed viscosity (Ghosh et al., 2013; Saxena et al., 2023; Steinberger & Calderwood, 2006) contrasts along plate boundaries were defined from Slab2.0 (Hayes et al., 2018). Mantle thermal heterogeneity was inferred from *S*-wave tomography (Tao et al., 2018), converted to temperature using BurnMan (Hightower et al., 2024; Myhill et al., 2023) with mineralogical and attenuation constraints (Anderson & Hart, 1978; Choi et al., 2006). Mantle rheology followed a composite flow law combining diffusion and dislocation creep (Hirth & Kohlstedt, 2003).

We designed four model suites (24 cases) to test the influence of plate boundary configuration and depth-dependent thermal heterogeneity on the stress field: (a) plate boundary activation or inactivation (Plate Boundary series), (b) truncation of anomalies either below specified depths (D-series) or above them (B-series), and (c) confinement to specific depth bands (BD-series) (Table S1 in Supporting Information S1). However, as the mantle flow system is non-linear and vertically coupled, removing anomalies from one depth range inevitably alters the overall buoyancy balance. We therefore acknowledge that these experiments do not strictly isolate contributions from different depths, but rather serve as depth-dependent sensitivity tests. All simulations employed free-slip boundary conditions at all model boundaries.

From each simulation, we derived stress tensor fields and calculated the azimuthal orientation of maximum horizontal stress (S_{max}). These were compared against stress orientations inverted from moment tensor solutions for 133 crustal earthquakes, using a standard focal-mechanism stress inversion workflow (Álvarez-Gómez, 2019; Hardebeck & Michael, 2006; Martínez-Garzón et al., 2014; Michael, 1984). Moment tensor solutions followed a time-windowed TDMT procedure akin to CAP and used a regional 1-D velocity model (S. Kim et al., 2011; Son et al., 2017; Templeton et al., 2008, Text S3 in Supporting Information S1). Additionally, we assessed the correlation between seismicity and modeled strain rate using an inhomogeneous Poisson point process (IPPP) framework (Ogata, 1998) applied to 375 crustal earthquakes from the Korea Meteorological Administration (KMA) declustered catalog, with model fitting and validation implemented in the *spatstat* package in R (Baddeley et al., 2016, Text S4 in Supporting Information S1).

Further methodological details—including governing equations, rheological laws, tomography-to-thermodynamics conversion, seismic waveform analysis, and statistical model fitting—are provided in Texts S1–S4 in Supporting Information S1.

3. Results

Detailed descriptions and results for all 24 model scenarios (the four suites of models) are provided in Texts S5, S6, and Figures S7–S14 in Supporting Information S1. Here we highlight representative findings, focusing on crustal strain rate patterns and orientations of S_{max} ($\theta_{S_{max}}$) under varying plate boundary configurations (Figures 2a–2c and 3a–3c) and different depths of upper-mantle heterogeneity (Figures 2d–2i and 3d–3i).

3.1. Plate Boundary Configurations

In the base case, the KP shows highest strain along its margins, with rates near $\sim10^{-15.8}$ s^{-1} offshore west of Jeju Island (JI) and the southwest coast, tapering inland to $\sim10^{-16.3}$ s^{-1} (Figure 2a). With only the PS boundary active, the overall pattern persists but with weaker magnitudes, especially in the northern West Sea (WS) ($\sim10^{-16.1}$–$10^{-16.2}$ s^{-1}, Figure 2b). When no plate boundaries are prescribed as weak, deformation decreases further (Figure 2c). Thus, omitting subduction interfaces lowers overall strain but does not erase the fundamental margin-interior contrast.

The $\theta_{S_{max}}$ also depend on boundary configuration (Figures 3a–3c). With both PA and PS included, the field is relatively uniform: ENE–WSW compression dominates the west, while the east rotates gradually from E–W in the south to WNW–ESE in the north (Figure 3a). Under PS-only configuration, the same pattern holds with a slight clockwise rotation in the eastern side (Figure 3b). Without weak boundaries, the west still trends ENE–WSW, but along the eastern coast stress axes swing nearly N–S (Figure 3c).

3.2. Depth-Dependent Thermal Structure

The distribution of strain varies strongly with the depth extent of mantle buoyancy sources. In the shallowest case (D50), deformation is uniformly low ($\sim10^{-17.0}$–$10^{-16.0}$ s^{-1}) (Figure 2d). As anomalies extend deeper, strain localizes along the coasts. In D400, enhanced strain ($\sim10^{-15.9}$ s^{-1}) appears south and east of Korea, while the northwest remains weak ($\sim10^{-16.5}$–$10^{-16.2}$ s^{-1}, Figure 2e). At D600, a N–S belt of higher strain develops along the west, and the east-central interior becomes a low-strain corridor (Figure 2f). The full-depth base case sharpens this pattern, with maximum strain on the western and southern margins and minima through the east-central peninsula (Figure 2a). These trends suggest that transition-zone buoyancy anomalies exert significant control on where crustal strain accumulates, favoring the coastal margins when such deep anomalies are present.

Complementary B-series experiments, which include only anomalies below a given depth, highlight the importance of vertical continuity. Models restricted to depths >300 km (B600–B400) produce minimal deformation ($<10^{-16.4}$ s^{-1}, Figure 2g). Adding shallower structure dramatically increases strain: in B150, broad areas reach $\sim10^{-15.9}$–$10^{-15.7}$ s^{-1} (Figure 2h). However, including very shallow anomalies (B100, B50) redistributes and in places reduces strain rates, in central Korea and much of the WS and ES domains (Figure 2i). Thus, while deep buoyancy alone is ineffective, upward extension into the upper mantle amplifies crustal deformation, but the shallowest density contrasts can counteract these effects.

The depth-dependent thermal structure also influences the modeled stress orientations (Figures 3d–3i). With only shallow anomalies (D50), orientations are highly scattered (Figure 3d). As heterogeneity extends to mid-mantle

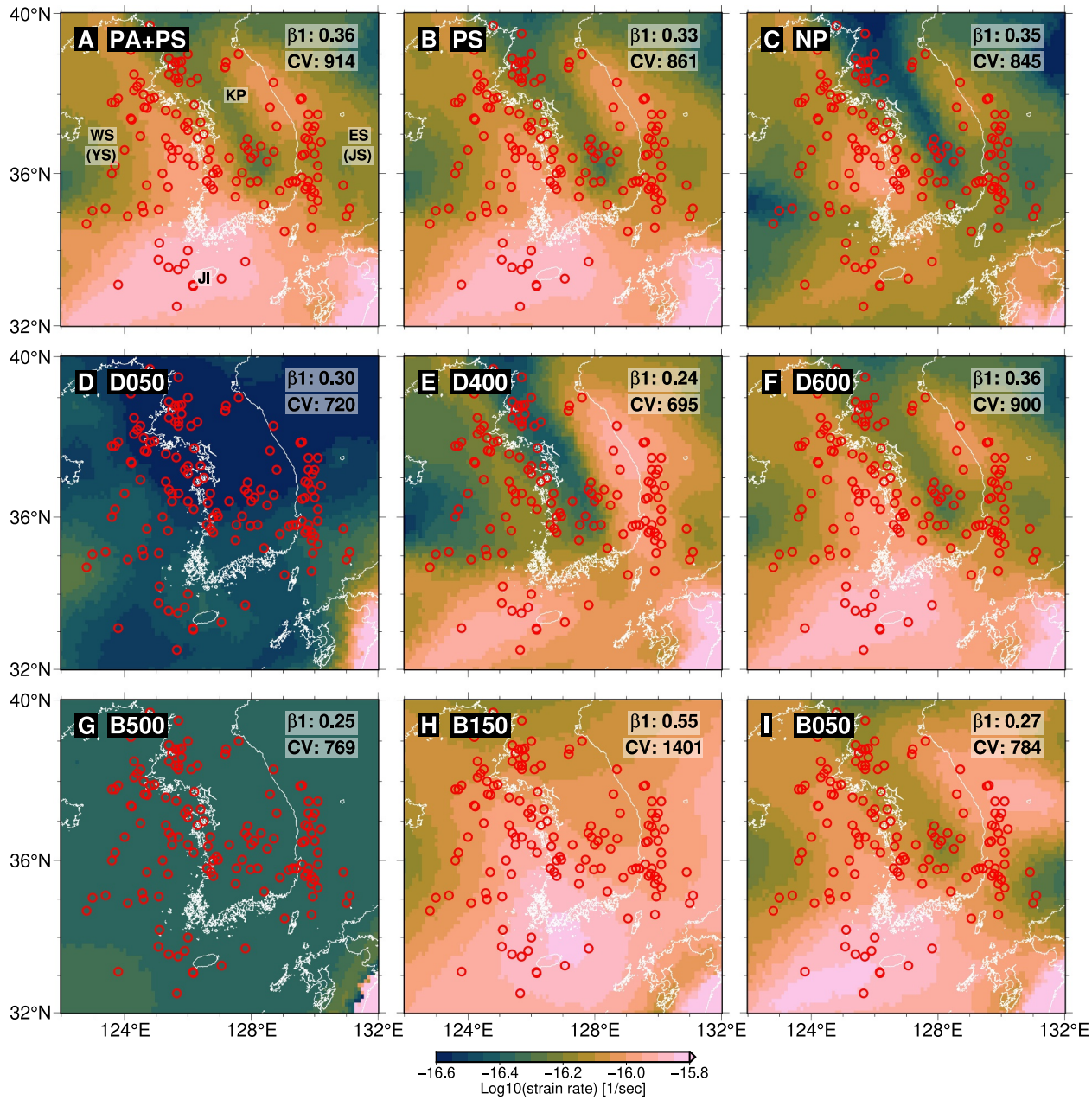

Figure 2. Spatial distribution of strain rate at a depth of 25 km in the Korean Peninsula for representative model cases: (a) PA + PS (base case), (b) PS-only, (c) no-boundary (NP) case, (d) D050, (e) D400, (f) D600, (g) B500, (h) B150, and (i) B050. Red circles indicate the distribution of earthquakes with magnitudes ≥3.5 from the Korea Meteorological Administration catalog (1978–2024). Geographic references–KP: Korean Peninsula, WS: West Sea (YS: Yellow Sea), ES: East Sea (JS: Sea of Japan), and JI: Jeju Island.

depths (D100–D400), the west and south develop consistent ENE–WSW compression, while the east remains N–S to NNE–SSW (Figure 3e). Inclusion of transition-zone anomalies (D600, base) aligns the eastern stress field with the west, producing a coherent E–W regime (Figure 3f). From the bottom-up perspective, deep-only models (B500) yield a uniform NNE–NE trend (Figure 3g). Adding shallower structure (B150) rotates the field clockwise, bringing most of the peninsula into E–W compression (Figure 3h). Subsequent inclusion of the shallowest anomalies (B100, B50) preserves this pattern (Figure 3i). Collectively, models lacking either shallow or deep buoyancy generate variable orientations, whereas full-depth heterogeneity—especially including the subducted slab—produces a stable E–W to ENE–WSW directed tectonic stress across the KP.

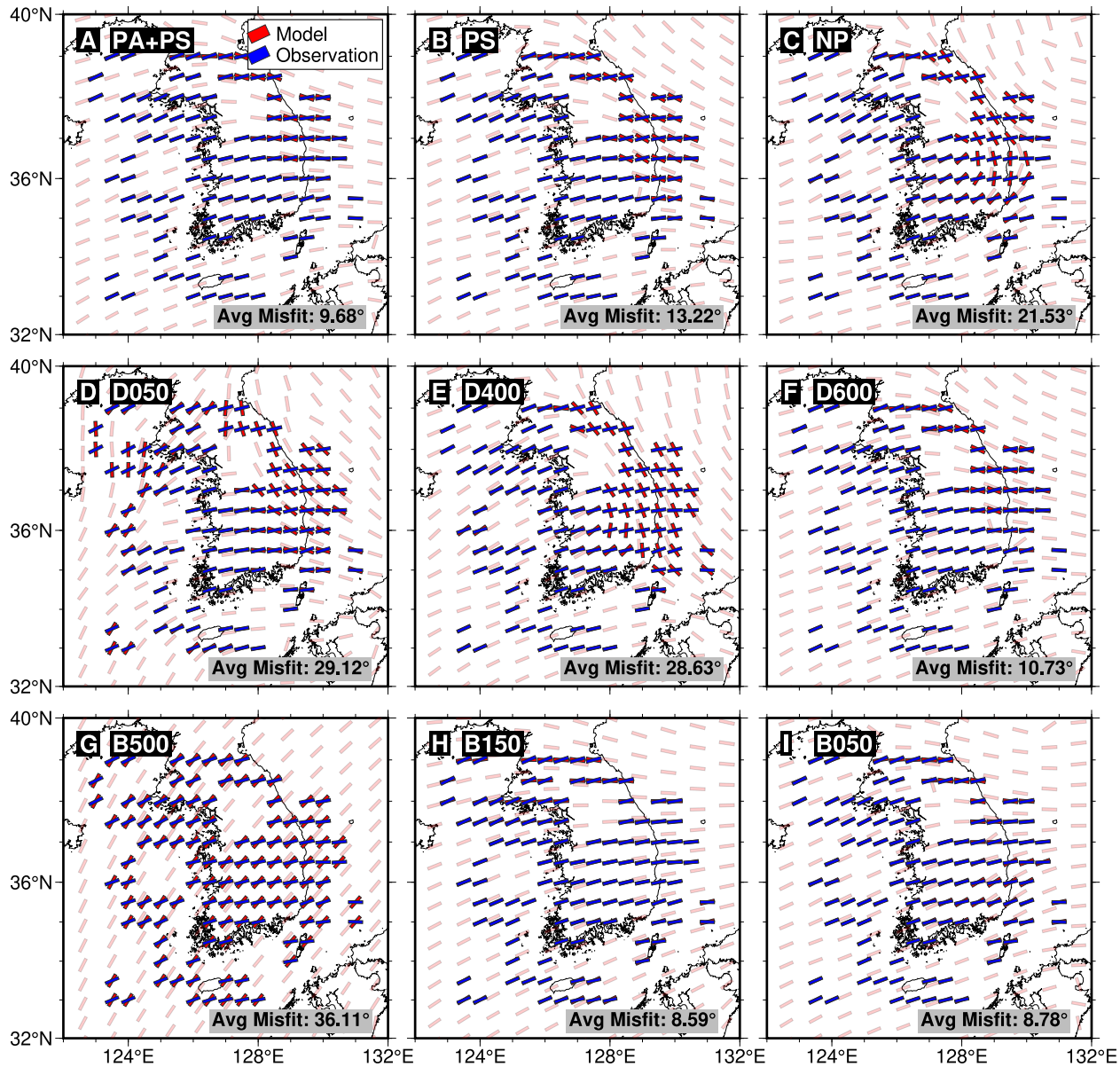

Figure 3. Orientation of S_{max} at a depth of 25 km across the Korean Peninsula for the same cases as Figure 2: (a) PA + PS (base) case, (b) PS-only case, (c) NP case, (d) D050 case, (e) D400 case, (f) D600 case, (g) B500 case, (h) B150 case, and (i) B050 case. Red bars show modeled S_{max} orientations; blue bars in each panel show observed S_{max} from stress inversion of regional earthquakes. Nearest-neighbor matching was applied to compare modeled orientations with observations, and transparency was applied to model vectors in regions without corresponding observations.

3.3. Observed $\theta_{S_{max}}$ From Stress Inversion

The observed $\theta_{S_{max}}$, derived from stress inversion of regional moment tensor solutions, are shown as blue lines in Figure 3. Across the KP, the western peninsula and WS exhibit ENE–WSW orientations, while the eastern peninsula and ES are closer to E–W.

3.4. Inhomogeneous Poisson Point Process Results

IPPP modeling quantifies the strain rates–seismicity spatial association and predictive generalizability across all 24 scenarios (Figures 4a and 4b). The strain rate coefficient (β_1) indicates the correlation strength, Z-scores measure statistical significance, and cross-validation (CV) error evaluates generalizability. Full results are in Table S2 in Supporting Information S1.

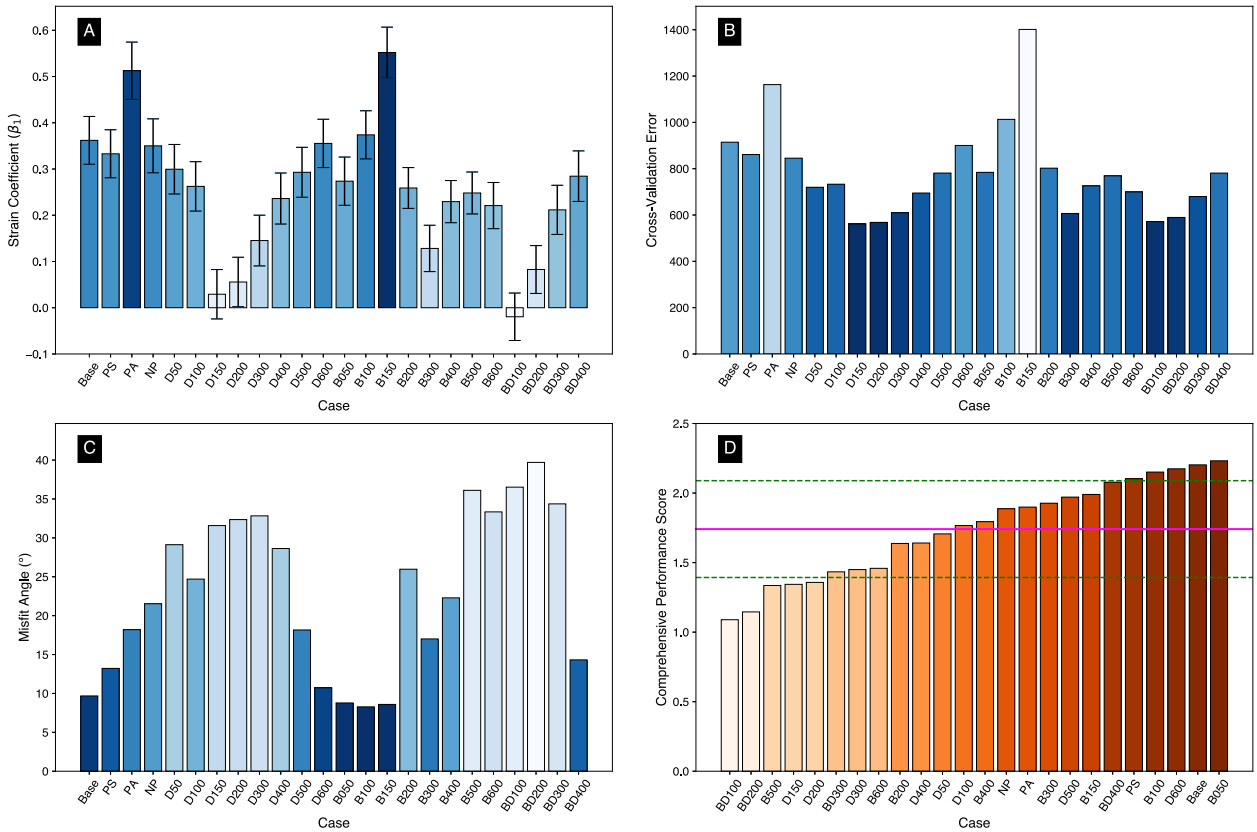

Figure 4. Results of inhomogeneous Poisson point process modeling across 24 geodynamic scenarios. (a) Estimated strain rate coefficients (β_1) with ±1 standard error bars, representing the strength of spatial association between modeled strain rate and earthquake occurrence. (b) Cross-validation (CV) errors for each scenario. (c) Estimated angular misfit between modeled and observed stress orientations. (d) Comprehensive performance score for each scenario, defined as the sum of normalized β_1, CV error, and misfit angle, with the latter two metrics subtracted from unity to reflect their lower-is-better interpretation. Scenarios include variations in plate boundary configurations (Base, PS, PA, and NP) and thermal heterogeneity truncation depths (D50–D600, B50–B600, and BD100–D400). The magenta line denotes the median score (1.741), and green dashed lines indicate ±1 standard deviation (0.348).

The base case (PA + PS) yields $\beta_1 = 0.362$ (Z-score: $Z = 7.01$) and a CV error of 914.38 (Figures 4a and 4b and Table S2 in Supporting Information S1). The PS-only case produced a coefficient of 0.333 ($Z = 6.41$) and a CV error of 861.15. The PA-only case showed the highest coefficient (0.513, $Z = 8.29$), but also the highest CV error (1163.10). The NP returned a coefficient of 0.350 ($Z = 6.00$) and a CV error of 845.43. All four cases exceeded a Z-score of 4.9, thereby indicating statistical significance at $p < 0.001$.

In the D-series, shallow models (D50–D100) achieve significant coefficients ($\beta_1 = 0.262$–0.300, $Z \geq 4.9$) with moderate CV errors (~720). Mid-depth truncations (D150–D400) produce low or insignificant correlations ($\beta_1 \leq 0.24$, $Z < 4.9$) despite low CV errors (~560–695). Deep cases (D500–D600) again show significant coefficients ($\beta_1 = 0.293$–0.355, $Z > 5.4$) with higher CV (~780–900).

In the B-series, most scenarios yield significant correlations. The strongest is B150 ($\beta_1 = 0.552$, $Z = 10.1$), though with the highest CV error (1401). B50 and B100 provide moderate coefficients (0.27–0.37) with acceptable CV (~780–1013). B200–B500 show varying performance, with B200 significant but modest ($\beta_1 = 0.259$), while B300 is insignificant ($\beta_1 = 0.128$), and B600 falls below significance ($\beta_1 = 0.221$, $Z = 4.43$).

The BD-series, which focuses on mid–upper mantle windows, generally performs poorly. Only BD400 reaches significance ($\beta_1 = 0.285$, $Z = 5.2$, CV = 781). Shallower BD100–BD300 cases yield weak or insignificant coefficients.

4. Discussion and Summary

4.1. Controls on Strain Rate and Stress Orientation in the Korean Peninsula

The spatial distribution of strain rates and $\theta_{S_{max}}$ across the KP responds systematically to variations in both plate boundary configurations and depth-dependent thermal structures. The observed $\theta_{S_{max}}$ patterns are consistent with prior studies (Rhie & Kim, 2010; Soh et al., 2018). While the expanded spatial coverage and quantitative assessment used in this study enable a more detailed comparison across model cases, we note that our quantitative validation is primarily driven by the dense inland data set, as offshore regions exhibit higher uncertainties due to sparse coverage (Figure S6 in Supporting Information S1). We summarize model performance with a composite score that combines three normalized quantities—the β_1 and CV error, and the angular misfit between modeled and observed $\theta_{S_{max}}$ (Figure 4).

Across the ensemble, the four model sets yield distinct insights into the sources of KP's stress. Weak zones associated with the PA and PS subduction systems exert a first-order control: their absence leads to suppressed strain rates and misaligned stress axes, as evident in the cases with different plate boundary configurations (Figures 2a–2c and Figures 3a–3c). While the NP model yields a β_1 comparable to Base (0.350 vs. 0.362), its misfit angle is substantially larger (21.5° vs. 9.68°), indicating that weak zones are critical for reproducing observed $\theta_{S_{max}}$ (Figures 4a and 4c). The PS-only model reduces the average misfit angle to 13.9°, outperforming the PA-only case (18.2°), and more accurately captures $\theta_{S_{max}}$.

The D-series demonstrates that deeper-seated buoyancy anomalies enhance model performance compared to shallower-only cases. Configurations limited to the upper transition zone (D50–D300) fail to reproduce coherent stress fields and seismicity, yielding large misfits ≥28° and low β_1 values (≤0.29) (Figures 4a–4c). In contrast, D500 and D600 markedly improve alignment (β_1 = 0.293 and 0.355; misfits = 18.2° and 10.7°), producing among the highest scores within the D-series (Figure 4d). These results highlight the potential importance of transition-zone anomalies in shaping the KP stress field, although their sufficiency requires further evaluation through the B-series.

The B-series directly addresses this by testing models with and without shallow buoyancy. Configurations restricted to deep sources (B300–B600) perform poorly, whereas adding shallower anomalies (B100, B150) substantially improves results, with higher β_1 values (0.374 and 0.552) and lower misfits (~8°–9°) despite larger CV errors (≈1,013–1,401) (Figures 4a–4c). The best overall balance is achieved in B050 (misfit = 8.78°, β_1 = 0.274, CV = 784.2), which also ranks among the top-scoring models (Figure 4d). The BD-series reinforces this conclusion: models limited to mid–upper mantle structure alone yield poor performance, confirming that only vertically integrated buoyancy structures reproduce the observed stress field. Although vertical coupling prevents a strict separation of depth-dependent contributions, the contrasting model responses constrain the dynamic mechanism: the D-series identifies the deep mantle as a driver, while the B- and BD-series confirm the upper mantle as the stress channel required to transmit these forces to the surface.

These structural insights provide a framework for evaluating relative model performance. Rather than singling out a "best" model, we highlight a subset of top performers with scores above $\mu + \sigma = 2.089$ ($\mu = 1.741$, $\sigma = 0.348$) (Figure 4d). Five models—B050 (2.232), Base (2.203), D600 (2.175), B100 (2.151), and PS (2.103)—fall within this range. The strong performance of the PS model indicates the importance of weak subduction interfaces. Because the density structure and prescribed weak-interface viscosity are identical across the PS and PA cases, its greater influence compared to the PA system reflects its closer proximity to the KP, although variations in real-world coupling strength along slab interfaces could alter this conclusion. The Base model performs nearly as well as B050, suggesting that incorporating the full structural complexity still provides meaningful value. Notably, B050 scored slightly better than Base and B100, indicating that adding the anomalies in 50–100 km depth range improved performance, while including 0–50 km anomalies reduced it. This implies that density variations in the shallow lithosphere, or at least in its uppermost part, may not contribute constructively—and could even interfere with—model performance.

These results highlight that intraplate deformation across the KP is explained by the combined effects of mantle-derived buoyancy forces (Becker et al., 2015; Ghosh & Holt, 2012; Ghosh et al., 2013; Hightower et al., 2024; Lithgow-Bertelloni & Guynn, 2004; Saxena et al., 2021) coupled with weak subduction interfaces and temperature-dependent variations in lithospheric density, viscosity, and thickness (Bott et al., 2024; Cao &

Liu, 2024; S. Lee et al., 2022, 2025; Mooney et al., 2012) at depths greater than ~50 km. However, our constraints on shallow lithospheric buoyant contributions are limited by the CRUST1.0 representation, and we cannot exclude local stress modulation by unresolved fine-scale density contrasts and thermomechanical contribution (Bott et al., 2024; Levandowski et al., 2017).

Our study adds to the insights from the previous work on the origin of stress distribution in the KP. Earlier works highlighted the role of lithospheric thickness variations in controlling deformation across the southern Korean Peninsula (SKP) (S. Lee et al., 2022, 2025). One such study analyzed GNSS-derived deformation rates following the 2011 Tohoku-Oki earthquake and proposed that the year-5 field approximates the background interseismic strain after postseismic relaxation (S. Lee et al., 2025). Comparing this field with our B050 model reveals broad agreements in strain magnitudes (order of 10^{-15} s^{-1}) and spatial patterns, particularly along the eastern and southwestern coasts. However, discrepancies in the central SKP likely reflect unmodeled shallow lithospheric variations and residual postseismic signals in the GNSS data. Including such small-scale structure in future work may improve the fit.

The spatial patterns of strain rate in our Base, B050, and NP models remain broadly compatible with those of S. Lee et al. (2022), reinforcing that upper mantle heterogeneity is a dominant driver of regional deformation in the KP. However, a key distinction lies in the driving mechanism for the $\theta_{S_{max}}$. Their best-fit model relied on 50 MPa of imposed E–W compression to reproduce the observed stress field, but this uniform boundary condition reduced the spatial correlation with seismicity. In contrast, this study demonstrates that such imposed simplified boundary tractions are unnecessary if the full-depth buoyancy structure—including the stagnant slab—and mechanically weak subduction interfaces (PA and PS) are considered. However, this does not rule out far-field stresses (e.g., Zoback, 1992), as intraplate fields are controlled by the complex interplay of mantle buoyancy, lithospheric strength, and boundary forces. Thus, rather than being negligible, far-field forces likely require self-consistent global modeling to be rigorously integrated (e.g., Hightower et al., 2024; Saxena et al., 2023), as uniform boundary conditions remain insufficient to capture such complexity.

4.2. Stress Rotation Associated With the Cold Slab in Mantle Transition Zone?

Structural heterogeneities within the KP's upper mantle add complexity to the regional stress environment. The dense, flattened, and deflected Pacific slab beneath Northeast Asia has been imaged as a high-velocity anomaly in numerous regional and global tomographic studies (Fukao et al., 1992; Huang & Zhao, 2006; Y. Kim et al., 2021; S.-H. Lee et al., 2014; Obayashi et al., 2006, 2009, 2013; Schaeffer & Lebedev, 2013; Tang et al., 2014; Tao et al., 2018; van der Hilst et al., 1991; Xi et al., 2024; Zhao, 2004). While Gorbatov and Kennett (2003) suggested that a long, flattened slab segment beneath the Izu–Bonin region may reflect chemical heterogeneity based on *P*-wave images, they noted that these features were not evident in *S*-wave images. In contrast, both *P*-wave (e.g., Zhao, 2004) and *S*-wave (e.g., Tao et al., 2018) images consistently show high-velocity anomalies associated with the stagnant slab beneath the KP (Figures 1c and 1d).

A global SS precursor study by Flanagan and Shearer (1998) showed the 660 km discontinuity to be most depressed (~20 km) in the northwestern Pacific. Using teleseismic *P*-wave receiver functions, S.-H. Lee et al. (2014) imaged a similar depression beneath the KP, with the discontinuity 15–20 km deeper and the deepest portions located between 128°E and 130°E. This depression becomes shallower westward (S.-H. Lee et al., 2014), a pattern also observed by Sun et al. (2020), suggesting a thermal origin and a concentration of cold material along the eastern margin of the KP. Although another hypothesis for the stagnant slab involves mantle wind (Peng et al., 2021), this mechanism does not account for the observed temperature-dependent depression.

Our observations suggest that these colder, denser slab structures in the mantle transition zone function as a gravitational sinker. While this cold slab appears to correspond to Stage I proposed by Fukao and Obayashi (2013), it likely represents a transient state preceding slab penetration into the lower mantle. During this stage, the slab may continue to exert a downward pull on the surrounding mantle, inducing vertical flow that produces compressive forces in the overlying lithosphere (Figure S15 in Supporting Information S1). This compression mechanism is consistent with the E–W $\theta_{S_{max}}$ observed in the eastern KP. This interpretation is further supported by synthetic tests (Text S7 and Figure S16 in Supporting Information S1), which confirm that deep-seated negative buoyancy is sufficient to enhance crustal compression along the eastern margin.

In summary, this study provides a physically grounded model for intraplate deformation across the KP by linking upper-mantle buoyancy forces with mechanically weak subduction interfaces. We find that observed $\theta_{S_{max}}$ and seismicity can be explained without invoking imposed boundary tractions, as assumed in earlier work (S. Lee et al., 2022), provided that both the PA and PS subduction systems are incorporated and that vertically coherent buoyant structures are present. Notably, our results highlight the role of the Pacific slab in the mantle transition zone as a gravitational source that enhances crustal compression in the eastern KP, consistent with the observed east–west $\theta_{S_{max}}$. In the absence of this cold slab, such compressive forces are not reproduced in our models, implying that the slab may be locally sinking by depressing the transition zone, despite appearing stagnant in tomographic images (e.g., Zhao, 2004).

Our models, while informative, have several limitations. These include: (a) omission of surface topography and associated isostatic adjustments, (b) assumption of an incompressible upper mantle, (c) lack of explicit incorporation of phase transitions, (d) exclusion of minor tectonic features such as pre-existing faults within the KP, and (e) use of the instantaneous formulation that represents the present-day mechanical equilibrium. Future studies addressing these factors may refine or extend our findings. Nevertheless, the consistent performance of structurally distinct models—such as B050, Base, and D600—demonstrates that large-scale thermal and mechanical architecture effectively explains the observed $\theta_{S_{max}}$ and seismicity across the KP.

Conflict of Interest

The authors declare no conflicts of interest relevant to this study.

Data Availability Statement

All data and materials needed to reproduce the results are available as follows. The earthquake catalog is available from the KMA at https://www.weather.go.kr/neng/earthquake/earthquake-korea.do. Seismic waveform data are provided through the FDSN service at the KIGAM Quake portal (https://data.kigam.re.kr/quake/data/web-services) and are freely available after registration. Seismic velocity models: IRIS Earth Model Collaboration (EMC), http://ds.iris.edu/ds/products/emc/. Data is available at S. Lee and Cho (2025).

Acknowledgments
This work was supported by the Basic Research Project (GP2025-012) of the Korea Institute of Geoscience and Mineral Resources (KIGAM), funded by the Ministry of Science and ICT (MSIT), Republic of Korea. Y. Kim was supported by the National Research Foundation of Korea Grant (MSIT) (RS-2022-NR070842). ChatGPT was occasionally used to assist in refining sentence structures and improving the clarity of this manuscript. We thank the handling editor, Dr. Fabio A. Capitanio, and two anonymous reviewers for constructive feedback.

References

Álvarez-Gómez, J. A. (2019). FMC—Earthquake focal mechanisms data management, cluster and classification. *SoftwareX*, *9*, 299–307. https://doi.org/10.1016/j.softx.2019.03.008

Anderson, D. L., & Hart, R. S. (1978). Q of the Earth. *Journal of Geophysical Research*, *83*(B12), 5869–5882. https://doi.org/10.1029/JB083iB12p05869

Arvidsson, R. (1996). Fennoscandian earthquakes: Whole crustal rupturing related to postglacial rebound. *Science*, *274*(5288), 744–746. https://doi.org/10.1126/science.274.5288.744

Baddeley, A., Rubak, E., & Turner, R. (2016). *Spatial point patterns: Methodology and applications with R*. CRC Press.

Baird, A. F., McKinnon, S. D., & Godin, L. (2010). Relationship between structures, stress and seismicity in the Charlevoix seismic zone revealed by 3-D geomechanical models: Implications for the seismotectonics of continental interiors. *Journal of Geophysical Research*, *115*(B11), B11405. https://doi.org/10.1029/2010JB007521

Bangerth, W., Dannberg, J., Fraters, M., Gassmöller, R., Glerum, A., Heister, T., et al. (2023). Aspect 2.5.0 [Software]. *Zenodo*. https://doi.org/10.5281/zenodo.8200213

Becker, T. W., Lowry, A. R., Faccenna, C., Schmandt, B., Borsa, A., & Yu, C. (2015). Western US intermountain seismicity caused by changes in upper mantle flow. *Nature*, *524*(7566), 458–461. https://doi.org/10.1038/nature14867

Bird, P. (2003). An updated digital model of plate boundaries. *Geochemistry, Geophysics, Geosystems*, *4*(3), 1027. https://doi.org/10.1029/2001GC000252

Bott, J., Scheck-Wenderoth, M., Kumar, A., Cacace, M., Noe, S., & Faleide, J. I. (2024). Density and strength variations in the mantle lithosphere affect the distribution of intraplate earthquakes. *Communications Earth & Environment*, *5*(1), 1–14. https://doi.org/10.1038/s43247-024-01417-4

Calais, E., Freed, A. M., Van Arsdale, R., & Stein, S. (2010). Triggering of New Madrid seismicity by late-Pleistocene erosion. *Nature*, *466*(7306), 608–611. https://doi.org/10.1038/nature09258

Cao, Z., & Liu, L. (2024). Western US intraplate deformation controlled by the complex lithospheric structure. *Nature Communications*, *15*(1), 3917. https://doi.org/10.1038/s41467-024-48223-2

Choi, S. H., Mukasa, S. B., Kwon, S.-T., & Andronikov, A. V. (2006). Sr, Nd, Pb and Hf isotopic compositions of late Cenozoic alkali basalts in South Korea: Evidence for mixing between the two dominant asthenospheric mantle domains beneath East Asia. *Chemical Geology*, *232*(3–4), 134–151. https://doi.org/10.1016/j.chemgeo.2006.02.014

Di Giacomo, D., Engdahl, E. R., & Storchak, D. A. (2018). The ISC-GEM earthquake catalogue (1904–2014): Status after the extension project. *Earth System Science Data*, *10*(4), 1877–1899. https://doi.org/10.5194/essd-10-1877-2018

Flanagan, M. P., & Shearer, P. M. (1998). Global mapping of topography on transition zone velocity discontinuities by stacking SS precursors. *Journal of Geophysical Research*, *103*(B2), 2673–2692. https://doi.org/10.1029/97jb03212

Fuchs, L., & Becker, T. W. (2022). On the role of rheological memory for convection-driven plate reorganizations. *Geophysical Research Letters*, *49*(18), e2022GL099574. https://doi.org/10.1029/2022GL099574

Fukao, Y., & Obayashi, M. (2013). Subducted slabs stagnant above, penetrating through, and trapped below the 660 km discontinuity. *Journal of Geophysical Research: Solid Earth*, *118*(11), 5920–5938. https://doi.org/10.1002/2013JB010466

Fukao, Y., Obayashi, M., Inoue, H., & Nenbai, M. (1992). Subducting slabs stagnant in the mantle transition zone. *Journal of Geophysical Research*, *97*(B4), 4809–4822. https://doi.org/10.1029/91JB02749

Ghosh, A., & Holt, W. E. (2012). Plate motions and stresses from global dynamic models. *Science*, *335*(6070), 838–843. https://doi.org/10.1126/science.1214209

Ghosh, A., Holt, W. E., & Wen, L. (2013). Predicting the lithospheric stress field and plate motions by joint modeling of lithosphere and mantle dynamics. *Journal of Geophysical Research: Solid Earth*, *118*(1), 346–368. https://doi.org/10.1029/2012JB009516

Gorbatov, A., & Kennett, B. L. N. (2003). Joint bulk-sound and shear tomography for western Pacific subduction zones. *Earth and Planetary Science Letters*, *210*(3–4), 527–543. https://doi.org/10.1016/S0012-821X(03)00165-1

Hao, M., Li, Y., & Zhuang, W. (2019). Crustal movement and strain distribution in east Asia revealed by GPS observations. *Scientific Reports*, *9*(1), 16797. https://doi.org/10.1038/s41598-019-53306-y

Hardebeck, J. L., & Michael, A. J. (2006). Damped regional-scale stress inversions: Methodology and examples for southern California and the Coalinga aftershock sequence. *Journal of Geophysical Research*, *111*(B11), B11310. https://doi.org/10.1029/2005JB004144

Hayes, G. P., Moore, G. L., Portner, D. E., Hearne, M., Flamme, H., Furtney, M., & Smoczyk, G. M. (2018). Slab2, a comprehensive subduction zone geometry model. *Science*, *362*(6410), 58–61. https://doi.org/10.1126/science.aat4723

Heister, T., Dannberg, J., Gassmöller, R., & Bangerth, W. (2017). High accuracy mantle convection simulation through modern numerical methods – II: Realistic models and problems. *Geophysical Journal International*, *210*(2), 833–851. https://doi.org/10.1093/gji/ggx195

Heki, K. (2003). Snow load and seasonal variation of earthquake occurrence in Japan. *Earth and Planetary Science Letters*, *207*(1–2), 159–164. https://doi.org/10.1016/S0012-821X(02)01148-2

Hightower, E., Gurnis, M., & Mao, W. (2024). Influence of Farallon slab loading on intraplate stress and seismicity in eastern North America in the presence of pre-existing weak zones. *Geochemistry, Geophysics, Geosystems*, *25*(6), e2024GC011493. https://doi.org/10.1029/2024GC011493

Hirth, G., & Kohlstedt, D. (2003). Rheology of the upper mantle and the mantle wedge: A view from the experimentalists. In J. Eiler (Ed.), *Inside the subduction factory* (Vol. 138, pp. 83–105). American Geophysical Union. https://doi.org/10.1029/138GM06

Holford, S. P., Hillis, R. R., Hand, M., & Sandiford, M. (2011). Thermal weakening localizes intraplate deformation along the southern Australian continental margin. *Earth and Planetary Science Letters*, *305*(3–4), 207–214. https://doi.org/10.1016/j.epsl.2011.02.056

Huang, J., & Zhao, D. (2006). High-resolution mantle tomography of China and surrounding regions. *Journal of Geophysical Research*, *111*(B9), B09305. https://doi.org/10.1029/2005JB004066

Jin, S., Li, Z. C., & Park, P.-H. (2006). Seismicity and GPS constraints on crustal deformation in the southern part of the Korean Peninsula. *Geosciences Journal*, *10*(4), 491–497. https://doi.org/10.1007/BF02910442

Kim, S., Rhie, J., & Kim, G. (2011). Forward waveform modelling procedure for 1-D crustal velocity structure and its application to the southern Korean Peninsula. *Geophysical Journal International*, *185*(1), 453–468. https://doi.org/10.1111/j.1365-246X.2011.04949.x

Kim, Y., Chang, S., Witek, M., Ning, J., & Wen, J. (2021). S-velocity mantle structure of East Asia from teleseismic traveltime tomography: Inferred mechanisms for the Cenozoic intraplate volcanoes. *Journal of Geophysical Research: Solid Earth*, *126*(3), e2020JB020345. https://doi.org/10.1029/2020JB020345

Kreemer, C., Blewitt, G., & Klein, E. C. (2014). A geodetic plate motion and global strain rate model. *Geochemistry, Geophysics, Geosystems*, *15*(10), 3849–3889. https://doi.org/10.1002/2014GC005407

Kronbichler, M., Heister, T., & Bangerth, W. (2012). High accuracy mantle convection simulation through modern numerical methods. *Geophysical Journal International*, *191*(1), 12–29. https://doi.org/10.1111/j.1365-246X.2012.05609.x

Lambert, V., Lapusta, N., & Perry, S. (2021). Propagation of large earthquakes as self-healing pulses or mild cracks. *Nature*, *591*(7849), 252–258. https://doi.org/10.1038/s41586-021-03248-1

Laske, G., Masters, G., Ma, Z., & Pasyanos, M. (2013). Update on CRUST1.0 – A 1-degree global model of Earth's crust. In *EGU general assembly conference abstracts* (Vol. 15).

Lee, S., & Cho, C. S. (2025). ASPECT-based 3D mantle convection models and stress inversion data for the Korean Peninsula [Dataset]. *figshare*. https://doi.org/10.6084/m9.figshare.29125739.v2

Lee, S., Choi, E., Son, M., Song, S. G., & Gómez, D. D. (2025). Viscoelastic modelling reveals correlation between GNSS-derived deformation rates after the 2011 Tohoku-Oki earthquake and lithospheric thickness in the southern Korean Peninsula. *Geophysical Journal International*, *242*(1), ggaf182. https://doi.org/10.1093/gji/ggaf182

Lee, S., Saxena, A., Song, J.-H., Rhie, J., & Choi, E. (2022). Contributions from lithospheric and upper-mantle heterogeneities to upper crustal seismicity in the Korean Peninsula. *Geophysical Journal International*, *229*(2), 1175–1192. https://doi.org/10.1093/gji/ggab527

Lee, S.-H., Rhie, J., Park, Y., & Kim, K.-H. (2014). Topography of the 410 and 660 km discontinuities beneath the Korean Peninsula and southwestern Japan using teleseismic receiver functions. *Journal of Geophysical Research: Solid Earth*, *119*(9), 7245–7257. https://doi.org/10.1002/2014JB011149

Levandowski, W., Zellman, M., & Briggs, R. (2017). Gravitational body forces focus North American intraplate earthquakes. *Nature Communications*, *8*(1), 14314. https://doi.org/10.1038/ncomms14314

Lithgow-Bertelloni, C., & Guynn, J. H. (2004). Origin of the lithospheric stress field. *Journal of Geophysical Research*, *109*(B1), B01408. https://doi.org/10.1029/2003JB002467

Martínez-Garzón, P., Kwiatek, G., Ickrath, M., & Bohnhoff, M. (2014). MSATSI: A MATLAB package for stress inversion combining solid classic methodology, a new simplified user-handling, and a visualization tool. *Seismological Research Letters*, *85*(4), 896–904. https://doi.org/10.1785/0220130189

Michael, A. J. (1984). Determination of stress from slip data: Faults and folds. *Journal of Geophysical Research*, *89*(B13), 11517–11526. https://doi.org/10.1029/JB089iB13p11517

Mishra, O. P., & Zhao, D. (2003). Crack density, saturation rate and porosity at the 2001 Bhuj, India, earthquake hypocenter: A fluid-driven earthquake? *Earth and Planetary Science Letters*, *212*(3–4), 393–405. https://doi.org/10.1016/S0012-821X(03)00285-1

Mooney, W. D., Ritsema, J., & Hwang, Y. K. (2012). Crustal seismicity and the earthquake catalog maximum moment magnitude (Mcmax) in stable continental regions (SCRs): Correlation with the seismic velocity of the lithosphere. *Earth and Planetary Science Letters*, *357–358*, 78–83. https://doi.org/10.1016/j.epsl.2012.08.032

Myhill, R., Cottaar, S., Heister, T., Rose, I., Unterborn, C., Dannberg, J., & Gassmöller, R. (2023). BurnMan—A Python toolkit for planetary geophysics, geochemistry and thermodynamics. *Journal of Open Source Software*, *8*(87), 5389. https://doi.org/10.21105/joss.05389

Obayashi, M., Sugioka, H., Yoshimitsu, J., & Fukao, Y. (2006). High temperature anomalies oceanward of subducting slabs at the 410-km discontinuity. *Earth and Planetary Science Letters*, *243*(1–2), 149–158. https://doi.org/10.1016/j.epsl.2005.12.032

Obayashi, M., Yoshimitsu, J., & Fukao, Y. (2009). Tearing of stagnant slab. *Science*, *324*(5931), 1173–1175. https://doi.org/10.1126/science.1172496

Obayashi, M., Yoshimitsu, J., Nolet, G., Fukao, Y., Shiobara, H., Sugioka, H., et al. (2013). Finite frequency whole mantle P wave tomography: Improvement of subducted slab images. *Geophysical Research Letters*, *40*(21), 5652–5657. https://doi.org/10.1002/2013GL057401

Ogata, Y. (1998). Space-time point-process models for earthquake occurrences. *Annals of the Institute of Statistical Mathematics*, *50*(2), 379–402. https://doi.org/10.1023/A:1003403601725

Pavlis, N. K., Holmes, S. A., Kenyon, S. C., & Factor, J. K. (2012). The development and evaluation of the Earth gravitational model 2008 (EGM2008). *Journal of Geophysical Research*, *117*(B4), B04406. https://doi.org/10.1029/2011JB008916

Peng, D., Liu, L., Hu, J., Li, S., & Liu, Y. (2021). Formation of East Asian stagnant slabs due to a pressure-driven Cenozoic mantle wind following Mesozoic subduction. *Geophysical Research Letters*, *48*(18), e2021GL094638. https://doi.org/10.1029/2021GL094638

Powell, C. A., Bollinger, G. A., Chapman, M. C., Sibol, M. S., Johnston, A. C., & Wheeler, R. L. (1994). A seismotectonic model for the 300-kilometer-long eastern Tennessee seismic zone. *Science*, *264*(5159), 686–688. https://doi.org/10.1126/science.264.5159.686

Rhie, J., & Kim, S. (2010). Regional moment tensor determination in the southern Korean Peninsula. *Geosciences Journal*, *14*(4), 329–333. https://doi.org/10.1007/s12303-010-0038-9

Saxena, A., Choi, E., Powell, C. A., & Aslam, K. S. (2021). Seismicity in the central and southeastern United States due to upper mantle heterogeneities. *Geophysical Journal International*, *225*(3), 1624–1636. https://doi.org/10.1093/gji/ggab051

Saxena, A., Dannberg, J., Gassmöller, R., Fraters, M., Heister, T., & Styron, R. (2023). High-resolution mantle flow models reveal importance of plate boundary geometry and slab pull forces on generating tectonic plate motions. *Journal of Geophysical Research: Solid Earth*, *128*(8), e2022JB025877. https://doi.org/10.1029/2022JB025877

Schaeffer, A. J., & Lebedev, S. (2013). Global shear speed structure of the upper mantle and transition zone. *Geophysical Journal International*, *194*(1), 417–449. https://doi.org/10.1093/gji/ggt095

Soh, I., Chang, C., Lee, J., Hong, T.-K., & Park, E.-S. (2018). Tectonic stress orientations and magnitudes, and friction of faults, deduced from earthquake focal mechanism inversions over the Korean Peninsula. *Geophysical Journal International*, *213*(2), 1360–1373. https://doi.org/10.1093/gji/ggy061

Son, M., Cho, C. S., Shin, J. S., Rhee, H., & Sheen, D. (2017). Spatiotemporal distribution of events during the first three months of the 2016 Gyeongju, Korea, earthquake sequence. *Bulletin of the Seismological Society of America*, *108*(1), 210–217. https://doi.org/10.1785/0120170107

Steinberger, B., & Calderwood, A. R. (2006). Models of large-scale viscous flow in the Earth's mantle with constraints from mineral physics and surface observations. *Geophysical Journal International*, *167*(3), 1461–1481. https://doi.org/10.1111/j.1365-246X.2006.03131.x

Sun, M., Gao, S. S., Liu, K. H., & Fu, X. (2020). Upper mantle and mantle transition zone thermal and water content anomalies beneath NE Asia: Constraints from receiver function imaging of the 410 and 660 km discontinuities. *Earth and Planetary Science Letters*, *532*, 116040. https://doi.org/10.1016/j.epsl.2019.116040

Tang, Y., Obayashi, M., Niu, F., Grand, S. P., Chen, Y. J., Kawakatsu, H., et al. (2014). Changbaishan volcanism in northeast China linked to subduction-induced mantle upwelling. *Nature Geoscience*, *7*(6), 470–475. https://doi.org/10.1038/ngeo2166

Tao, K., Grand, S. P., & Niu, F. (2018). Seismic structure of the upper mantle beneath Eastern Asia from full waveform seismic tomography. *Geochemistry, Geophysics, Geosystems*, *19*(8), 2732–2763. https://doi.org/10.1029/2018GC007460

Tarayoun, A., Mazzotti, S., & Gueydan, F. (2019). Quantitative impact of structural inheritance on present-day deformation and seismicity concentration in intraplate deformation zones. *Earth and Planetary Science Letters*, *518*, 160–171. https://doi.org/10.1016/j.epsl.2019.04.043

Tary, J. B., Hobbs, R. W., Peirce, C., Lesmes, C., & Funnell, M. J. (2021). Local rift and intraplate seismicity reveal shallow crustal fluid-related activity and sub-crustal faulting. *Earth and Planetary Science Letters*, *562*, 116857. https://doi.org/10.1016/j.epsl.2021.116857

Templeton, D., Rodgers, A., Helmberger, D., & Dreger, D. (2008). Comparison of the cut-and-paste and full moment tensor methods for estimating earthquake source parameters. In *AGU fall meeting abstracts* (Vol. 2008, p. S41C-1864).

van der Hilst, R., Engdahl, R., Spakman, W., & Nolet, G. (1991). Tomographic imaging of subducted lithosphere below northwest Pacific island arcs. *Nature*, *353*(6339), 37–43. https://doi.org/10.1038/353037a0

Wang, M., & Shen, Z.-K. (2020). Present-day crustal deformation of continental China derived from GPS and its tectonic implications. *Journal of Geophysical Research: Solid Earth*, *125*(2), e2019JB018774. https://doi.org/10.1029/2019JB018774

Wesnousky, S. G., & Scholz, C. H. (1980). The craton: Its effect on the distribution of seismicity and stress in North America. *Earth and Planetary Science Letters*, *48*(2), 348–355. https://doi.org/10.1016/0012-821X(80)90198-3

Xi, Z., Chen, M., Wei, S. S., Li, J., Zhou, T., Wang, B., & Kim, Y. (2024). EARA2024: A new radially anisotropic seismic velocity model for the crust and upper mantle beneath East Asia and northwestern Pacific subduction zones. *Geophysical Journal International*, *239*(1), 914–935. https://doi.org/10.1093/gji/ggae302

Zhao, D. (2004). Global tomographic images of mantle plumes and subducting slabs: Insight into deep Earth dynamics. *Physics of the Earth and Planetary Interiors*, *146*(1–2), 3–34. https://doi.org/10.1016/j.pepi.2003.07.032

Zoback, M. L. (1992). First- and second-order patterns of stress in the lithosphere: The world stress map project. *Journal of Geophysical Research*, *97*(B8), 11703–11728. https://doi.org/10.1029/92JB00132